Inorganic Chemistry

pubs.acs.org/IC

Article

Construction of Ln^{3+}-Substituted Arsenotungstates Modified by 2,5-Thiophenedicarboxylic Acid and Application in Selective Fluorescence Detection of Ba^{2+} in Aqueous Solution

Dan Wang, Yamin Li, Yan Zhang, Xin Xu, Yong Liu, Lijuan Chen,* and Junwei Zhao*

Cite This: *Inorg. Chem.* 2020, 59, 6839–6848

Read Online

ACCESS | Metrics & More | Article Recommendations | Supporting Information

ABSTRACT: Developing organic–inorganic hybrid lanthanide(Ln)-functionalized polyoxometalates (POMs) has long been a main research topic. In this article, two novel hexameric Ln-containing arsenotungstates modified by 2,5-thiophenedicarboxylic acid (H_2tpdc) $[H_2N(CH_3)_2]_{21}Na_{13}\{Ln_6W_{14}O_{40}(H_2O)_{18}(Htpdc)_2\}[B\text{-}\alpha\text{-}AsW_9O_{33}]_6\cdot nH_2O$ [Ln = Eu^{3+}, n = 94 (**1Eu**); Ln = Gd^{3+}, n = 114 (**2Gd**)] were successfully obtained, and the sulfur-heterocyclic carboxylic acid ligand was for the first time introduced to the POM system. Both polyoxoanion skeleton structures can be regarded as an aggregation of six trivacant Keggin $[B\text{-}\alpha\text{-}AsW_9O_{33}]^{9-}$ entities linked by a *S*-shaped $[Ln_6W_{14}O_{40}(H_2O)_{18}(Htpdc)_2]^{20-}$ cluster. More surprisingly, two carboxyl O atoms in $Htpdc^-$ groups directly coordinate with two W atoms other than Ln atoms, which is rarely seen in tungsten-oxo clusters. Fluorescence properties of **1Eu** in solid state and aqueous solution have been systematically investigated. Also, **1Eu** as a fluorescence sensor in aqueous solution toward the detection of the Ba^{2+} ion has been explored. As expected, **1Eu** may be a promising fluorescence probe for the Ba^{2+} detection in the absence of Ca^{2+} or Sr^{2+} ions in aqueous environment with high sensitivity, good selectivity, and low detection limit (1.19×10^{-3} mM). This work not only first introduces the S-heterocyclic carboxylic acid ligand into the POM system and enriches the types of organic ligands which can be used in POM chemistry but also broadens the POMs' application in fluorescence detection.

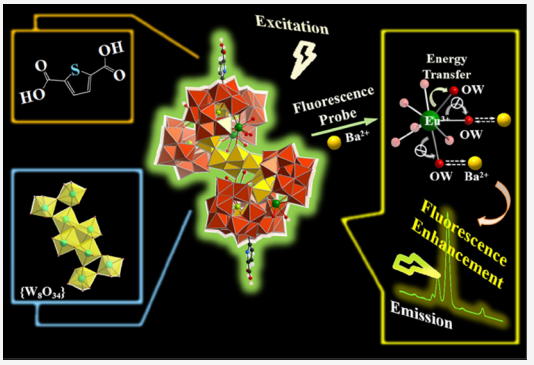

INTRODUCTION

Pursuing new functional metal–oxygen cluster materials has long been a goal of chemists and materials scientists due to extensive applications in different fields.[1−3] As an important branch of metal–oxygen clusters, polyoxotungstates (POTs) have appealed to a wide range of interests owing to their unique molecular structures, available molecular design and assembly, as well as their broad application prospects in catalysis,[4−7] sensing,[8−12] energy storage,[13−16] biomedicine,[17,18] and so on. Therefore, tremendous efforts have been devoted to constructing lanthanide (Ln) and/or transition-metal (TM) functionalized POTs with interesting structures,[19−24] which may generate unexpected application potentials in magnetism,[25−28] proton conductivity,[29,30] luminescence materials,[31,32] and catalysis.[33,34] A great deal of research has proved that heteroatom-inserted POTs, especially for arsenotungstates (ATs), can be assembled to novel giant poly(POT) clusters because of their highly reactive building blocks with abundant structural types.[35] Moreover, lacunary AT fragments can be also self-polymerized to larger aggregates (e.g., $[As_6W_{65}O_{217}(H_2O)_7]^{26-}$ (Figure 1a)).[36]

Since the groundbreaking multinuclear Ce^{3+}-substituted AT $[Ce_{16}(H_2O)_{36}(B\text{-}\alpha\text{-}AsW_9O_{33})_{12}(WO_2)_4(W_2O_6)_8(W_5CeO_{18})_4]^{76-}$ was reported by Pope in 1997 (Figure 1b),[37] Ln-containing ATs (LCATs) have been widely studied. Notably, the larger ion radii, diverse coordination numbers, and various coordination geometries of Ln cations greatly contribute to construct innovative LCATs,[38−41] such as $([(H_2O)_{11}Ln(Ln_2OH)(B\text{-}\alpha\text{-}AsO_3W_9O_{30})_4(WO_2)_4]^{20-}$ (Ln = Ce^{3+}, Nd^{3+}, Sm^{3+}, Gd^{3+}), $[M^m(H_2O)_{10}(Ln_2OH)_2(B\text{-}\alpha\text{-}AsO_3W_9O_{30})_4(WO_2)_4]^{(18-m)-}$ (Ln = La^{3+}, Ce^{3+}, Gd^{3+}; M = Ba^{2+}, K^+, Figure 1c),[39] $[Gd_8As_{12}W_{124}O_{432}(H_2O)_{22}]^{60-}$ (Figure 1d),[40] and $[Ln_{16}As_{16}W_{164}O_{576}(OH)_8(H_2O)_{42}]^{80-}$ (Ln = Eu^{3+}, Gd^{3+}, Tb^{3+}, Dy^{3+}, Ho^{3+}; Figure 1e).[41] These examples have proved that Ln^{3+} ions can not only integrate different AT building blocks together but also endow resulting LCATs with luminescence properties originating from eminent photoluminescence behaviors of Ln^{3+} cations (Figure 1f).[42,43] Furthermore, judicious introduction of organic components, especially for those with carboxyl groups, can effectively suppress the hydrolysis of Ln^{3+} ions and lead to the formation

Received: January 21, 2020
Published: May 7, 2020

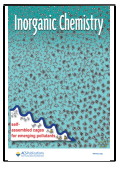

https://dx.doi.org/10.1021/acs.inorgchem.0c00223
Inorg. Chem. 2020, 59, 6839–6848

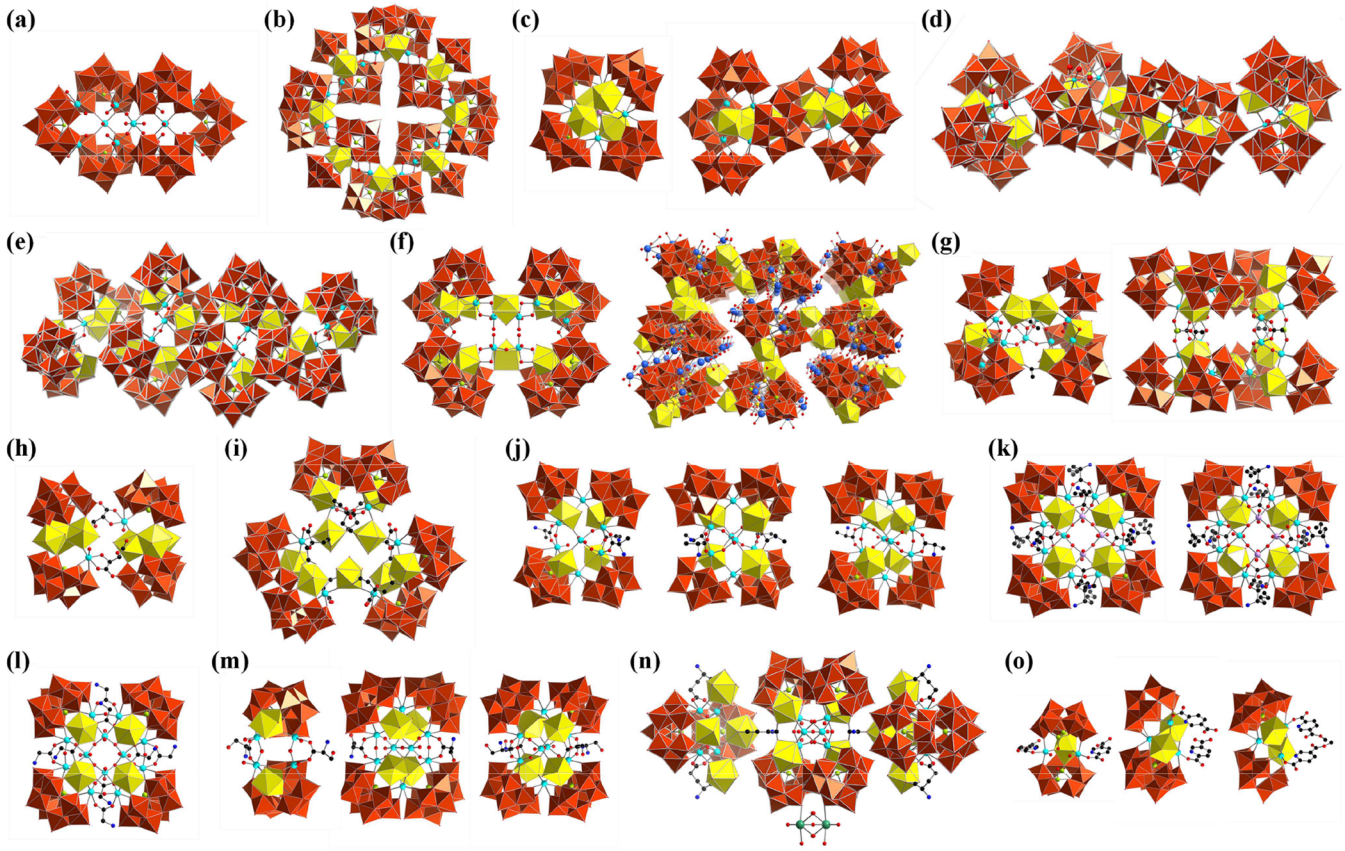

Figure 1. Some typical AT (a) and LCAT (b–o) structures reported in recent years.[12,36,37,39−50] Color code: W, turquoise; O, red; As, lime; C, black; N, blue; K, light blue; Ba, rose; {WO_6} octahetra, brownish red; {LnO_x} polyhedra, yellow.

of crystalline LCAT species. What's more, introducing organic components can also enhance the structural stability of desired LCAT species. As a result, persistent preparation and construction of organic–inorganic hybrid mutli-nuclear LCATs with novel structures and intriguing properties have been a subject of intensive research in the past two decades. Hitherto, some carboxylic-ligand-functionalized LCATs have been reported by Boskovic's group and Niu's group. In 2009, Boskovic's group obtained the first two acetate-functionalized high-nuclear LCATs $[Gd_6As_6W_{65}O_{229}(OH)_4(H_2O)_{12}(OAc)_2]^{38-}$ and $[Yb_{10}As_{10}W_{88}O_{308}(OH)_8(H_2O)_{28}(OAc)_4]^{40-}$ (Figure 1g).[44] After that, Niu et al. successively obtained a series of LCATs modified by flexible carboxylic ligands (for example, tartaric acid Figure 1h[45] and citric acid Figure 1i[46]). In addition, some amino acids (alanine, Figure 1j;[12] norleucine, Figure 1k;[47] glycine, Figure 1l;[47] serine, Figure 1m;[48] glutamic acid, Figure 1n;[49] and so on) with their variety of side chains have also been investigated to functionalize LCATs. By contrast, LCATs functionalized by rigid carboxylic acids are much less reported, and to date, available reports mainly involve pyridine-/pyrazine-based carboxylic acid ligands. The typical examples are 2,5-pyridine-dicarboxylic acid (H_2pdc) and 5-(methoxycarbonyl)-2-pyridine-carboxylic acid (Hmcpc) decorated LCATs $[Y\{AsW_8O_{30}\}_2(AsO)_2\{WO_2(pdc)\}_2]^{13-}$ and $[\{Y(H_2O)_3\}_2\{As_2W_{19}O_{68}\}\{WO_2(L)\}_2]^{8-}$ (L = Hpdc or mcpc) (Figure 1o) reported by Boskovic in 2013.[50]

Up to now, various flexible or rigid organic ligands have been used in reported LCATs (Table S1) with potential applications in electrochemical sensing,[12] magnetism,[45] luminescence,[48,49] catalysis,[51] and antibacterial activity.[52] However, thiophenecarboxylic acids or their derivatives have not been reported in construction and functionalization of LCATs, even though they have some advantages from the strong coordination ability of heteratom (S atom) and carboxylic oxygen atoms, which are believed to catch different tungsten–oxygen building blocks or various metal centers, which contribute to form novel and steady structures. Therefore, 2,5-thiophenedicarboxylic acid (H_2tpdc) and Ln^{3+} ions are chosen as the functional components to modify in situ generated AT fragments in this work for the purpose of discovering novel organic–inorganic hybrid mutli-nuclear LCATs with interesting properties. To further expand the research on organic–inorganic hybrid LCATs and develop potential fluorescent probe materials for detecting trace metal ions in a water environment, we have successfully prepared two Htpdc$^-$-modified LCATs $[H_2N(CH_3)_2]_{21}Na_{13}\{Ln_6W_{14}O_{40}(H_2O)_{18}(Htpdc)_2\}[B\text{-}\alpha\text{-}AsW_9O_{33}]_6{\cdot}nH_2O$ [Ln = Eu^{3+}, n = 94 (**1Eu**); Ln = Gd^{3+}, n = 114 (**2Gd**)], whose polyoxoanion (POA) skeleton structures are constructed from an *S*-shaped $[Ln_6W_{14}O_{40}(H_2O)_{18}(Htpdc)_2]^{20-}$ cluster connecting six trivacant Keggin $[B\text{-}\alpha\text{-}AsW_9O_{33}]^{9-}$ entities. It is worth emphasizing that the sulfur-heterocyclic carboxylic acid is first introduced into POMs, and carboxylic groups together with Ln^{3+} ions and adventitious W centers act as connectors in the hexameric structures of **1Eu** and **2Gd**. Interestingly, even though Ln^{3+} ions and organic ligands are removed away from their POA skeleton structures, six $[B\text{-}\alpha\text{-}AsW_9O_{33}]^{9-}$ entities are still connected by tungsten–oxygen groups by sharing vertexes or edges, which has rarely been reported before.[36,39,50]

https://dx.doi.org/10.1021/acs.inorgchem.0c00223
Inorg. Chem. 2020, 59, 6839–6848

Luminescence properties of **1Eu** in solid state and aqueous solution have been systematically studied. **1Eu** has been also used as a fluorescence (FL) probe to explore its FL sensing properties toward detecting different metal ions. Experimental results indicate that **1Eu** can display a good recognition response toward detecting the Ba^{2+} ion in the absence of Ca^{2+} or Sr^{2+} ions in aqueous system.

RESULTS AND DISCUSSION

Synthesis. **1Eu** and **2Gd** were triumphantly synthesized through a one-step assembly reaction method based on simple starting materials such as $Na_2WO_4{\cdot}2H_2O$, As_2O_3, $Ln(NO_3)_3{\cdot}6H_2O$, H_2tpdc, and dimethylamine hydrochloride (DMA·HCl) in aqueous solution. In the synthesis process of **1Eu** and **2Gd**, several emphatic key points should be pointed out herein. First, the pH plays an important role in the preparation of **1Eu** and **2Gd**. Experimental results reveal that the optimum pH is about 3.80−3.90 for the crystal growth for **1Eu** and **2Gd**. When the pH is slightly lower than 3.80, the reaction solution becomes somewhat cloudy. The lower the pH, the more precipitates. This situation led to the failure of synthesizing the desired pure products. When the pH is in the range of 4.00−4.50, our previously reported LCATs $H_2N(CH_3)_2]_6Na_{24}H_{16}$-$\{[Ln_{10}W_{16}(H_2O)_{30}O_{50}](B\text{-}\alpha\text{-}AsW_9O_{33})_8\}{\cdot}97H_2O$ (Ln = Eu^{3+}, Gd^{3+}) were isolated.[53] As the pH is further higher than 4.50, we finally obtained some amorphous precipitates. Second, different Ln cations are also able to affect the formation of target compounds. When Ln^{3+} ions vary between La^{3+} and Nd^{3+} ions, or between Ho^{3+} and Lu^{3+} ions, those isostructural target compounds cannot be formed and only some amorphous mixtures were gained, which made us unable to determine their structures. When Ln^{3+} ions are Sm^{3+}, Eu^{3+}, Gd^{3+}, Tb^{3+}, or Dy^{3+} ions, respectively, the isomorphous products can come into being; to date, the crystal structures of only **1Eu** and **2Gd** have been determined because it is very difficult to grow good-quality single crystals of Sm^{3+}-, Tb^{3+}-, or Dy^{3+}-containing species. Our continuous efforts will be dedicated to cultivate their good-quality single crystals by systematically changing reaction conditions so that we can determine their crystal structures. Third, the usage of H_2tpdc is very crucial in the reaction procedure. In our experiment, when the usage of H_2tpdc is lower than 1.0 g, target compounds cannot be afforded. In addition, the comparisons of synthetic conditions of **1Eu** and **2Gd** with those previously reported LCATs are illustrated in Table S2. It can be apparently seen that the majority of previously reported LCATs were prepared by means of prefabricated AT precursors such as $[B\text{-}\alpha\text{-}AsW_9O_{33}]^{9-}$, $[As_2W_{19}O_{67}(H_2O)]^{14-}$, or $[(B\text{-}\alpha\text{-}AsO_3W_9O_{30})_4(WO_2)_4]^{28-}$, whereas the one-step assembly reaction method of simple tungstates, Ln^{3+} ions, and different heteroatom components was underdeveloped. Moreover, the divacant $[As_2W_{19}O_{67}(H_2O)]^{14-}$ precursor was the most widely used, possibly because it was the easiest accessible in comparison with other two AT precursors. The AT-precursor synthetic procedures are comparatively complicated due to the prefabrication of AT precursors, which prompts us to further develop the easier one-step synthetic strategy since the one-step synthetic strategy is extremely maneuverable, is not indispensable to synthesize AT precursors, and can simplify the experimental process. In this background, $NaAsO_2$, which can be simply obtained by dissolving As_2O_3 in NaOH solution, is supposed to be a wise heteroatom component.[12,42,48] The in situ flexible combination of $NaAsO_2$, $Na_2WO_4{\cdot}2H_2O$, and $Ln(NO_3)_3{\cdot}6H_2O$ in the reaction can provide a great possibility for constructing unpredictable LCATs. Besides, in contrast to those inorganic counter cations (such as Li^+, Na^+, K^+, Cs^+, Ba^{2+}, etc.), organic counter cations (e.g., protonated dimethylamine cations, protonated tetramethylamine cations, etc.) were utilized on account of their bigger volumes and can facilitate the stabilization of the large structures of resulting LCAT aggregates. According to our previous studies,[12,24,31,42,48] organic components (which here are DMA·HCl and H_2tpdc) can serve as organic solubilizers to, in some degree, improve the solubility of Ln^{3+} ions in the reaction system and enhance reactivities between different reaction materials. In the following times, with the aim of obtaining much more novel Ln-containing POTs and discovering some key points of synthesis and reaction assembly rules, we will proceed to thoroughly exploit the reaction systems including tungstates, Ln^{3+} ions, and different heteroatom components in the participation of various organic solubilizers by varying S/N-heterocyclic carboxylic acid ligands.

Structure Depiction. The phase purity of **1Eu** and **2Gd** has been confirmed by the good agreements of their PXRD patterns with simulated ones (Figure S1). **1Eu** and **2Gd** crystallize in the same crystal system with the $P\bar{1}$ space group (Table S3), where the results are also certified by complete similarities of their PXRD patterns and IR spectra (Figure S2). In this article, we take **1Eu** as an example to depict the crystal structure in detail. The molecular structure of **1Eu** consists of an organic−inorganic hybrid hexameric POA $\{Eu_6W_{14}O_{40}(H_2O)_{18}Htpdc)_2\}[B\text{-}\alpha\text{-}AsW_9O_{33}]_6^{34-}$ (**1a**) (Figure 2a), twenty-one monoprotonated $[H_2N(CH_3)_2]^+$ cations, 13 Na^+ ions, and ninety-four crystal waters. Bond valence sum (BVS) calculations manifest that the chemcial valences of W, As, and Ln atoms are +6, +3, and +3, respectfully (Table S4). The bowknot-like POA **1a** can be deemed as six trivacant Keggin $[B\text{-}\alpha\text{-}AsW_9O_{33}]^{9-}$ ($\{AsW_9\}$) subunits bridged by a *S*-shaped organic−inorganic hybrid $[Eu_6W_{14}O_{40}(H_2O)_{18}(Htpdc)_2]^{20+}$ (**1b**) heterometallic core containing six Eu^{3+} ions, 14 W^{VI} centers, and two $Htpdc^-$ ligands (Figure 2b).

The structure of the *S*-shaped heterometallic core **1b** can be seen as an assembly of 14 $\{WO_6\}$ octahedral groups bridged by six Eu^{3+} ions in the presence of two $Htpdc^-$ ligands (Figure 3a). When Eu^{3+} ions are taken away, **1b** can be divided into three parts, i.e., two isolated W2 centers, two $Htpdc^-$-bridging tungsten−oxygen dimers defined by W1 and W3 centers (denoted as {W1W3}), and an unseen central $\{W_8O_{34}\}$ cluster (Figure 3b). In detail, W1 and W3 centers are connected by two carboxyl O atoms from the $Htpdc^-$ ligand and a corner-sharing μ_2−O atom (O34) (the insert I in Figure 3b). The intriguing $\{W_8O_{34}\}$ cluster is formed by eight $\{WO_6\}$ octahedra by sharing vertexes or edges (the insert II in Figure 3b), which displays a chairlike structure (the insert III in Figure 3b). Upon close inspection to the inner junction of **1b**, when two organic ligands are removed away from **1b**, a purely inorganic $[Eu_6W_{14}O_{40}(H_2O)_{18}]^{22+}$ (**1c**) heterometallic core is formed (Figure 3c). Intriguingly, the *S*-shaped configuration of **1c** is still retained even without organic ligands. It can be explicitly observed from Figure 3c that **1c** shows a centrosymmetric structure, in which Eu^{3+} ions serve as supporting groups to hold up the whole skeleton. Concretely, the W2 center and the $Htpdc^-$-bridging {W1W3} dimer are connected together by $Eu2^{3+}$ and $Eu3^{3+}$ cations through sharing O atoms. Meanwhile, the W2 center and the $\{W_8O_{34}\}$ cluster are also connected by $Eu2^{3+}$ and $Eu3^{3+}$ cations through

https://dx.doi.org/10.1021/acs.inorgchem.0c00223
Inorg. Chem. 2020, 59, 6839−6848

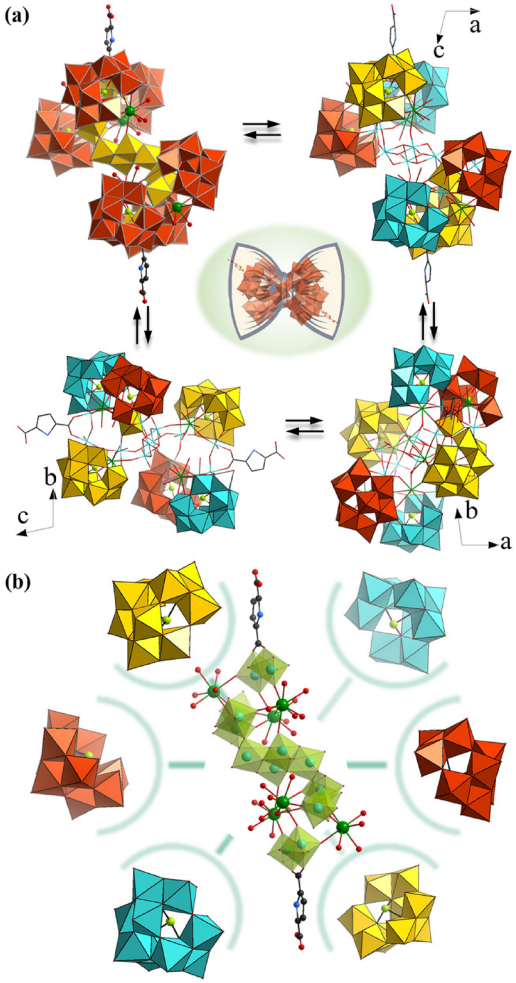

Figure 2. (a) View of the hexameric POA **1a** along different directions. (b) The breakdown drawing of **1a.** Color code: W, aqua; As, lime; O, red; S, light blue; Eu, green; C, black. The polyhedra of $\{AsW_9\}$ subunits are highlighted in different colors to distinguish $\{AsW_9\}$ subunits in different orientations in the POA skeleton of **1a**.

sharing O atoms. Besides, Eu1A^{3+}, Eu2^{3+}, and Eu3^{3+} centers work synchronously to join {W1W3} and $\{W_8O_{34}\}$ segments together (Figure 3c). In general, each of three Eu^{3+} ions is combined with three W centers (Eu1A^{3+}: W3, W5, W8A; Eu2^{3+}: W1, W2, W4; Eu3^{3+}: W1, W2, W4) by means of bridging O atoms (Figure 3d). The {Eu2Eu3W1W2W4} alignment can also be viewed as an irregular trigonal bipyramid, in which W1, W2, and W4 centers are located on the equatorial plane and Eu2 and Eu3 centers stand on two vertexes (the insert IV in Figure 3d). The Eu1A−W5−W3−W4−W1−Eu2 alignment also exhibits a twisted chair structure (the insert V in Figure 3d). In addition, three Eu^{3+} ions are all eight-coordinate with a distorted bicapped trigonal prismatic geometry (Figure 3e). In the Eu1^{3+} coordination sphere, O1WA and O76A occupy two cap sites [Eu1A−O: 2.310(17)−2.497(17) Å, ∠O−Eu1A−O: 67.9(6)−149.9(7)°]. In the Eu2^{3+} bicapped trigonal prismatic geometry, two water molecules (O5W and O6W) occupy two cap sites [Eu2−O: 2.294(16)−2.530(20) Å, ∠O−Eu2−O: 67.6(6)−147.9(6)°]. In the Eu3^{3+} coordination polyhedron, two cap sites are also taken up by two coordinated waters (O7W and O9W) [Eu3−O: 2.302(15)−2.514(18) Å, ∠O−Eu3−O: 66.5(5)− 147.9(6)°].

It is extremely noticeable that the obtained hexameric LCATs $\{[W_{14}Ln_6O_{40}(H_2O)_{18}(Htpdc)_2][B\text{-}\alpha\text{-}AsW_9O_{33}]_6\}^{34-}$ (Ln = Eu^{3+}, Gd^{3+}) in our work are the first examples of H_2tpdc-functionalized Ln-incorporated POMs. Interestingly, carboxylic groups only coordinate with W atoms, where the reason for which may be that the coordination between W centers and carboxyl O atoms of Htpdc$^-$ ligands has already occurred before introducing Ln^{3+} ions into the reaction system.

To achieve the charge balance and stabilize the structure, countercations such as Na$^+$ and $[H_2N(CH_3)_2]^+$ and lattice water molecules that surround **1a** POAs are necessary, and they can interact with **1a** POAs by hydrogen bonding and electrostatic interactions to form the 3-D supramolecular structure. To better understand the packing modes of **1a** POAs, Na$^+$ and $[H_2N(CH_3)_2]^+$ cations and lattice water molecules can be ignored, and each **1a** POA is simplified as a parallelogram along the *a*, *b* and *c* directions (Figure S3a−c). Apparently, **1a** POAs are aligned in a −AAA− stacking mode along each axial direction (Figure S3d−f), which can be explicitly seen in the schematic pictures (Figure S3g−i).

Luminescence Properties of Solid-State 1Eu. Ln^{3+} ions have abundant energy levels and 4f electrons can transit between different energy levels under excitation, endowing them promising photoluminescence properties. Therefore, LCATs in this work are supposed to exhibit outstanding FL properties. In order to find the optimal excitation wavelength of **1Eu**, the solid-state emission spectra of **1Eu** have been collected under different excitation wavelengths (λ_{ex}) varying from 250 to 500 nm (Figure 4a, Table S5). It can be clearly seen from the comparison that the emission spectrum of **1Eu** under excitation at 395 nm is the most intense, suggesting that the 395 nm excitation is the optimum excitation. At the same time, when exciting **1Eu** under different excitation wavelengths (λ_{ex} = 250−500 nm), the corresponding emission colors are also highlighted in the CIE chromaticity (Figure S4), from which we can obviously see that **1Eu** emits different colors under different excitation wavelengths, indicating that **1Eu** may be a color-tunable material by changing excitation wavelengths. Upon excitation at 395 nm, the solid-state emission spectrum of **1Eu** displays eight Eu^{3+} characteristic emission peaks (525 nm: $^5D_1 \rightarrow {}^7F_0$; 538 nm: $^5D_1 \rightarrow {}^7F_1$; 556 nm: $^5D_1 \rightarrow {}^7F_2$; 580 nm: $^5D_0 \rightarrow {}^7F_0$; 594 nm: $^5D_0 \rightarrow {}^7F_1$; 615 nm: $^5D_0 \rightarrow {}^7F_2$; 652 nm: $^5D_0 \rightarrow {}^7F_3$; 701 nm: $^5D_0 \rightarrow {}^7F_4$),[48,54] and the red emission at 615 nm is most prominent (Figure 4b). As we know, the appearance of the symmetry-forbidden $^5D_0 \rightarrow {}^7F_0$ emission (580 nm) illustrates that the Eu^{3+} ions inhabit the low-symmetrical coordination environment in **1Eu**.[55] Its excitation spectrum was measured and is provided in Figure S5. Besides, the lifetime decay curve obtained by supervising the $^5D_0 \rightarrow {}^7F_2$ transition can be fitted by the monoexponential function, and the afforded lifetime (τ) is 263.29 μs (Figure 4c).

As illustrated in Figure 4d, the partial overlapping of the oxygen-to-metal (O → W) charge transfer emission spectrum of AT fragments in **1Eu** and the excitation spectrum of Eu^{3+} ions is evidently observed, which can testify the occurrence of energy migration from AT fragments to Eu^{3+} ions in **1Eu**, that is, the oxygen-to-metal (O → W) charge transfer of AT fragments sensitize the FL emission of Eu^{3+} ions in **1Eu**.[54,56] This energy migration phenomenon can also be evidenced by the time-resolved emission spectroscopy (TRES) of **1Eu** (Figure 4e). It can be explicitly seen that the emission intensity

https://dx.doi.org/10.1021/acs.inorgchem.0c00223
Inorg. Chem. 2020, 59, 6839−6848

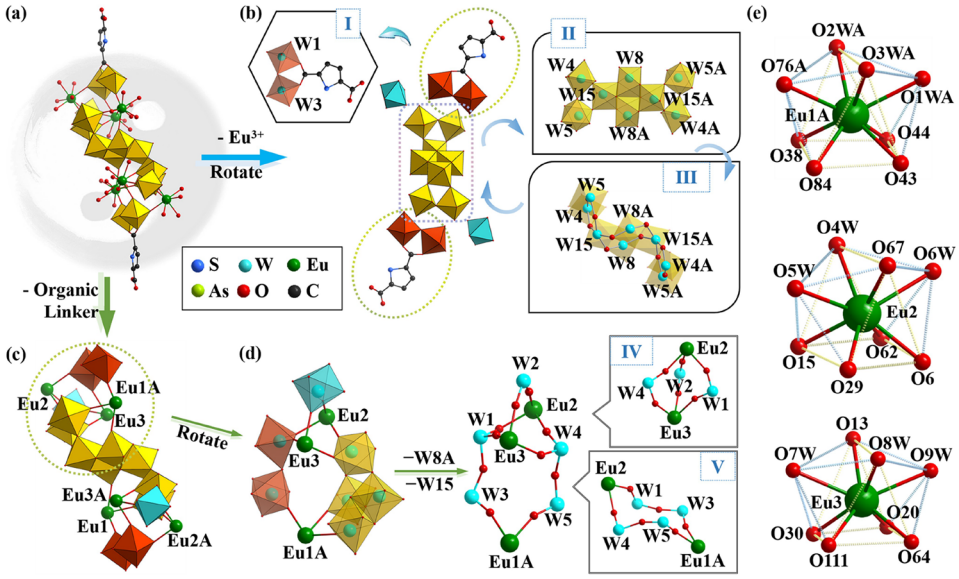

Figure 3. (a) The *S*-shaped **1b**. (b) The connection between $\{WO_6\}$ groups after removing away Eu^{3+} ions from **1b**. Insert I: The connection between W1 and W3. Inserts II and III: The bonding mode in central $\{W_8O_{34}\}$ cluster. Color code: $\{WO_6\}$ octahedra linking to $Htpdc^-$, brownish red; $\{WO_6\}$ octahedra in $\{W_8O_{34}\}$ cluster, gold; $\{WO_6\}$ octahedra bridging Eu2 and Eu3, aqua. (c) The pure-inorganic heterometallic core **1c** (some O atoms are omitted). (d) Simplified view of the half-unit of **1c**. Insert IV: The irregular trigonal bipyramid (Eu2−W2−W4−W1−Eu3). Insert V: The twisted chair structure (Eu1A−W5−W3−W4−W1−Eu2). (e) Coordination environments of eight-coordinate bicapped trigonal prismatic $Eu1^{3+}$, $Eu2^{3+}$, and $Eu3^{3+}$ ions. Color code: W, aqua; As, lime; O, red; S, light blue; Eu, green; C, black.

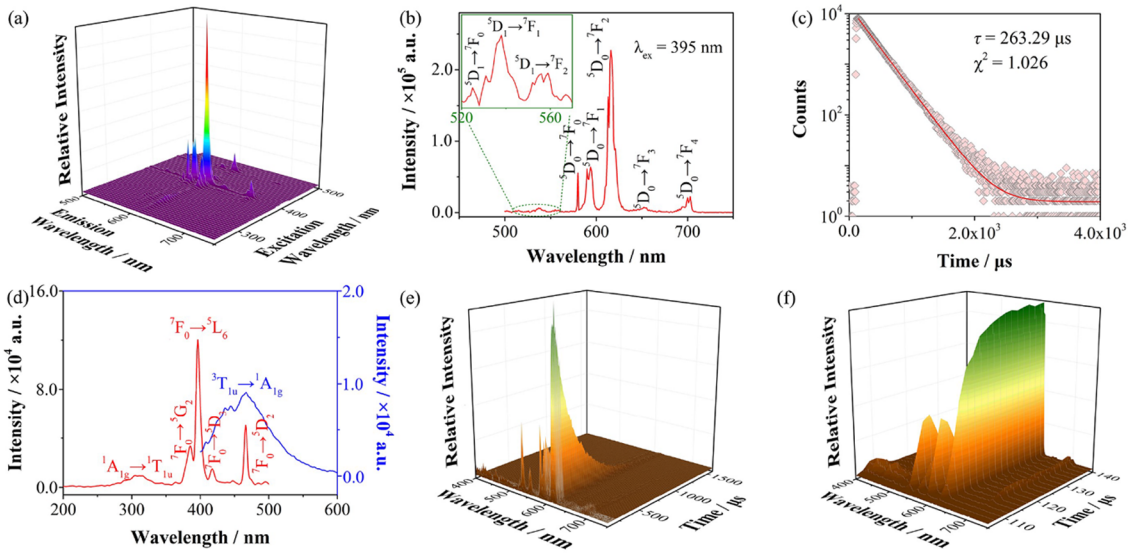

Figure 4. (a) Emission spectrograms of **1Eu** under different excitations (250−500 nm). (b) Emission spectrogram of **1Eu** (λ_{ex} = 395 nm). (c) Lifetime decay curve of the emission peak at 615 nm of **1Eu** (λ_{ex} = 395 nm). The red solid line is generated by fitting a monoexponential function. (d) The overlap of the emission spectrum of AT fragments (obtained by exciting **1Gd**, λ_{ex} = 310 nm) and the excitation spectrum of Eu^{3+} ions (obtained by exciting **1Eu**, λ_{ex} = 310 nm). (e) TRES profiles of **1Eu** (λ_{ex} = 310 nm) in the decay time range of 105.0−1585.4 μs. (f) TRES profiles of **1Eu** (λ_{ex} = 310 nm) in the decay time range of 105.0−140.0 μs.

of **1Eu** rises with increasing the excitation time and that the emission intensity of the $^3T_{1u} \rightarrow {}^1A_{1g}$ emission band derived from AT fragments reaches the maximum at 110 μs, while the emission intensity of Eu^{3+} ions arrives at the maximum at 140 μs (Figure 4f). After 140 μs, the $^3T_{1u} \rightarrow {}^1A_{1g}$ emission band almost cannot be observed and the emission intensity of Eu^{3+} ions gradually declines (Figure S6). This observation demonstrates that the harvested energy by AT fragments is transferred to Eu^{3+} ions for the FL emission. The energy-level scheme indicating energy migration from AT fragments to Eu^{3+} ions is displayed in Figure 5. Upon using the 395 nm light to irradiate **1Eu**, some of the light is absorbed by the $^7F_0 \rightarrow {}^5D_4$, $^7F_0 \rightarrow {}^5G_2$, $^7F_0 \rightarrow {}^5L_6$, $^7F_0 \rightarrow {}^5D_3$, and $^7D_0 \rightarrow {}^5D_2$ transitions of Eu^{3+} ions, giving rise to the characteristic emissions stemming from $^5D_1 \rightarrow {}^7F_0$, $^5D_1 \rightarrow {}^7F_1$, $^5D_1 \rightarrow {}^7F_2$, $^5D_0 \rightarrow {}^7F_0$, $^5D_0 \rightarrow {}^7F_1$, $^5D_0 \rightarrow {}^7F_2$, $^5D_0 \rightarrow {}^7F_3$, and $^5D_0 \rightarrow {}^7F_4$ transitions of Eu^{3+} ions,[48,54] whereas some of the light is absorbed by the $^1A_{1g} \rightarrow {}^1T_{1u}$ transition of AT segments.[56] Due to the spin−orbital coupling interaction, the electrons in the $^1T_{1u}$ state relax to the $^3T_{1u}$ state through a nonradiative

https://dx.doi.org/10.1021/acs.inorgchem.0c00223
Inorg. Chem. 2020, 59, 6839−6848

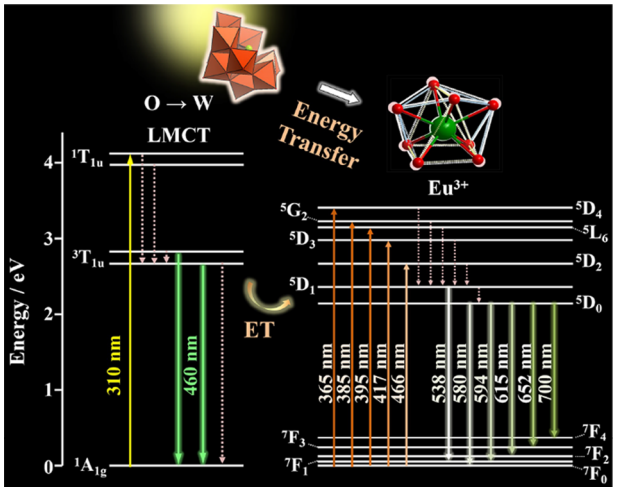

Figure 5. Energy-level scheme indicating energy migration from AT fragments to Eu^{3+} ions in **1Eu**. Solid lines are radiation processes, and dotted lines are nonradiative processes.

process. When the electrons the $^3T_{1u}$ state are back to the $^1A_{1g}$ ground state, producing the $^3T_{1u} \rightarrow {}^1A_{1g}$ emission, some of which are reabsorbed by the $^7F_0$ ground state of Eu^{3+} ions, bringing forth the energy migration from AT fragments to Eu^{3+} ions and sensitizing the emission of Eu^{3+} ions.

Luminescence Properties of 1Eu in Aqueous Solution. To study the luminescence behavior of **1Eu** in aqueous solution, its emission spectrum was collected under excitation at 395 nm (Figure 6a). Comparison of no remarkable changes in the position and shape of the characteristic emission peaks of **1Eu** in aqueous solution with those in solid-state **1Eu** (Figure 6a) proofs that the POA skeleton structure of **1Eu** may be stable in aqueous solution. Ulteriorly, the excitation spectrum was also tested under monitoring the emission at 615 nm (Figure S7), in which the excitation band around 310 nm ($^3T_{1u} \rightarrow {}^1A_{1g}$) of AT fragments can be clearly seen. More importantly, the emission intensity of AT fragments is almost constant (the insert in Figure S7), even though the luminescence emission intensity of Eu^{3+} ions decreases obviously, further certifying that the POA skeleton structure of **1Eu** may be stable in aqueous solution.[57] However, the decrease of emission intensity and the shortening of the decay time of **1Eu** in aqueous solution may be related to the occurrence of the dynamic exchange process between water ligands in Eu^{3+} ions in **1a** and water molecules in solution and to the dissociation of a small number of samples of **1a** in water.

The evolution of luminescence emission stability of **1Eu** in aqueous solution has been explored by monitoring the emission spectrum of **1Eu** in aqueous solution for 12 h. The luminescence emission intensity goes down rapidly in the first hour, then shows a slow decrease in the following 3 h (Figure 6b), and keeps almost unchanged after 4 h. As mentioned above, the dynamic exchange process between water ligands in Eu^{3+} ions in **1a** and water molecules in solution and the dissociation of a small number of samples of **1a** in water happen when **1Eu** is dissolved in water, which results in a noticeable decrease of the emission intensity, while this process has been accomplished after 4 h and the emission intensity remains almost unchanged. This speculation can be further confirmed by the observation that the luminescence decay lifetime of **1Eu** just being dissolved in water (τ_0 = 262.83 μs) is reduced to 253.36 μs after 4 h (Figure 6c, d). What's more, the effect of the luminescence behavior of **1Eu** in water with different pH values has also been surveyed (Figure 6e) and exhibits a good fluorescent stability in a wide pH range of 4.52−8.50. Moreover, the sensitization of AT fragments in water to the emission of Eu^{3+} ions has been also proved by the TRES profile (Figure S8), offering forceful evidence for the similar luminescence behavior of either **1Eu** in water or solid **1Eu**. These results provide a precondition for **1Eu** as a fluorescence sensor for detecting metal ions in water,

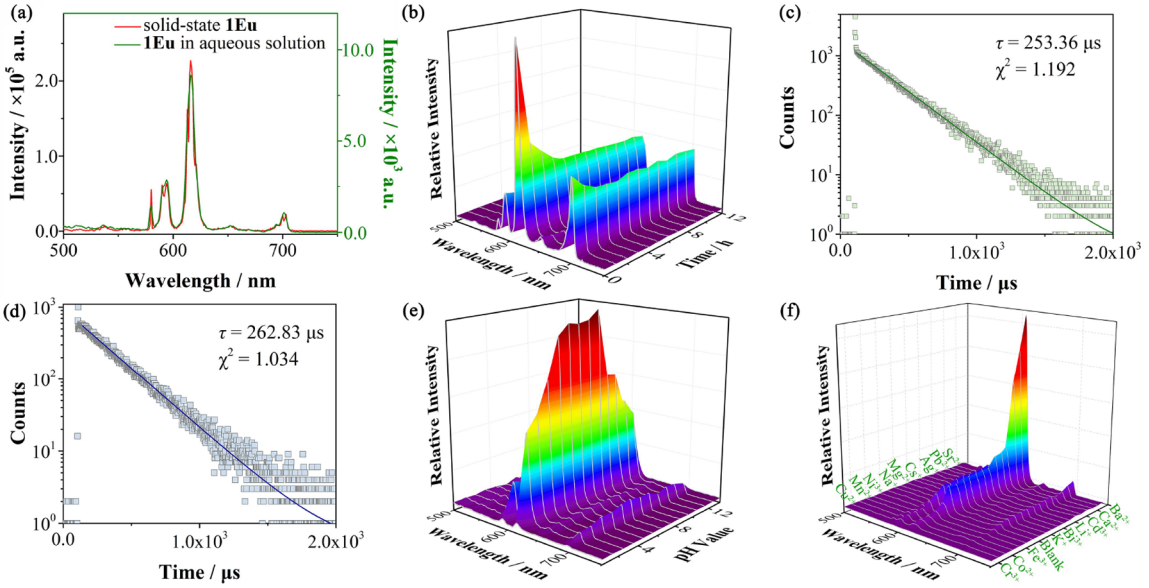

Figure 6. (a) Comparison of emission spectra of solid **1Eu** and **1Eu** in aqueous solution. (b) Evolution of emission spectra of **1Eu** in aqueous solution with time. (c, d) Lifetime decay curves of the emission peak at 615 nm of **1Eu** after being dissolved in water for 0 h (c) and 4 h (d). (e) Evolution of emission spectra of **1Eu** in aqueous solution with the pH. (f) PL emission spectra of **1Eu** in aqueous solution containing different metal ions (1.00 mM) (λ_{ex} = 395 nm).

https://dx.doi.org/10.1021/acs.inorgchem.0c00223
Inorg. Chem. 2020, 59, 6839−6848

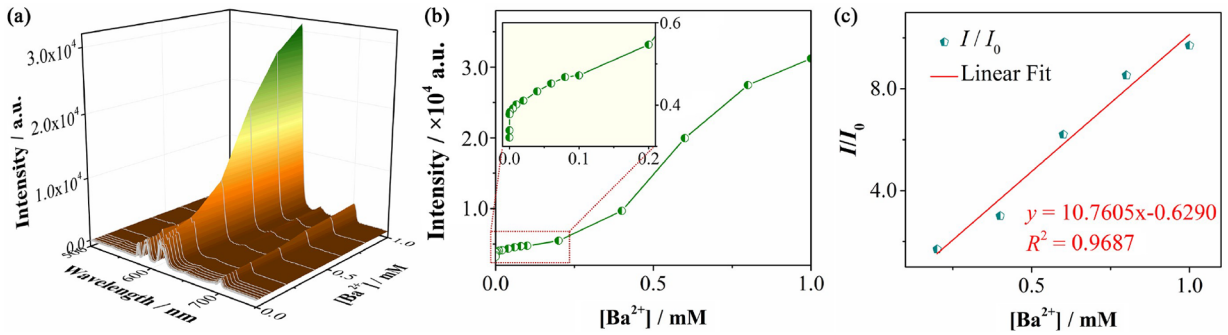

Figure 7. (a) Variation of FL emission spectra of **1Eu** with the concentration of Ba^{2+} ions in the varying range of 0−1.00 mM. (b) Variation of the emission peak intensity of **1Eu** at 615 nm with the concentration of Ba^{2+} ions in the varying range of 0−1.00 mM. (c) The linear fitting of I/I_0 ($[Ba^{2+}]$ = 0.20−1.00 mM).

manifesting that **1Eu** can be used as a FL probe in aqueous solution.

FL Sensing Performances of 1Eu in Aqueous Solution. The potential applications of Ln^{3+}-inserted materials as FL sensors for detecting metal ions in aqueous solution have captured rising research attention due to their excellent luminescent performances, good selectivity, and high stability.[58−60] Therefore, **1Eu** can be used to be a fluorescent probe material, and FL sensing properties of **1Eu** toward different metal ions have been systematically explored. Importantly, during FL sensing measurements, the pH values of solutions containing **1Eu** and different metal ions fall in the range of 4.50−4.70, so that **1Eu** remains stable in the whole process. As expected, FL intensity changes of **1Eu** in the solutions containing **1Eu** and different metal ions have taken place (Figure 6f). Apparently, the presence of Ca^{2+}, Sr^{2+}, or Ba^{2+} ions can in different degrees enhance the emission intensity of **1Eu**. The FL enhancement in the presence of the Ba^{2+} ion is the most obvious, and the FL emission intensity of **1Eu** at 615 nm has increased seven times in comparison with the case without the Ba^{2+} ion. Therefore, **1Eu** can work as a FL sensing probe toward the detection of the Ba^{2+} ion in the absence of Ca^{2+} or Sr^{2+} ions in aqueous solution. As a result, only the FL sensing of **1Eu** toward the detection of the Ba^{2+} ion was systematically researched in this article.

To further investigate the FL response of **1Eu** toward the Ba^{2+} ion, the FL emission spectra of **1Eu** in aqueous solution with different Ba^{2+} concentrations (0−1.00 mM (mM = mmol L^{-1})) have been systematically tested (Figure 7a); it can be seen from the results that the FL emission intensity of **1Eu** is gradually enhanced when the Ba^{2+} concentration $[Ba^{2+}]$ varies from 0.20 mM to 1.00 mM, whereas there was no significant enhancement in the FL emission intensity when the Ba^{2+} concentration changed in the range of 0−0.20 mM. As shown in Figure 7b, the strongest emission peak intensity at 615 nm also shows a similar variation trend. We fit the relationship between I/I_0 and $[Ba^{2+}]$ (0.20−1.00 mM), affording a linear regression equation of $y = 10.7605x - 0.6290$ (the linear correlation $R^2 = 0.9687$) (Figure 7c) (I represents the emission peak intensity at 615 nm of **1Eu** in the presence of different Ba^{2+} concentrations, and I_0 represents the emission peak intensity at 615 nm of **1Eu** in the absence of the Ba^{2+} ion). The limit of detection (LOD) is calculated to be 1.19×10^{-3} mM (LOD = $3s/k$, where s means the standard deviation of blank samples and k is the slope of the linear equation) (Table S6),[61] which is much lower than the Environmental Protection Agency (EPA) limit of the Ba^{2+} ion in drinking water (2.00 mg/L), indicating a good FL sensing potential (some representative research studies on the FL detection toward the Ba^{2+} ion are summarized in Table S7). Interestingly, the FL decay lifetime of **1Eu** in aqueous solution is prolonged while introducing the Ba^{2+} ion (Table S8). Therefore, a possible sound explanation for the sensing process may be that the interactions between Ba^{2+} ions and coordinated water molecules in **1a** are stronger than that between Eu^{3+} ions and coordinated water molecules, which weakens energy dissipation from Eu^{3+} ions to coordinated water molecules and leads to a strengthened FL emission.

Selectivity, as one of the significant evaluation indicators for a FL probe, was also examined herein by introducing various anions or cations into the solution containing the Ba^{2+} ion (0.10 mM). It is gratifying that either anions (NO_3^-, CH_3COO^-, Cl^-, and OH^-) or most cations (Li^+, Na^+, K^+, Cs^+, NH_4^+, Ag^+, Mg^{2+}) hardly influence the detection of the Ba^{2+} ion, while the emission intensity enhancement effect of **1Eu** can be accumulated in the coexistence of Ba^{2+} and Ca^{2+}/Sr^{2+} ions (Figure 8). This observation can exhibit that **1Eu** as a

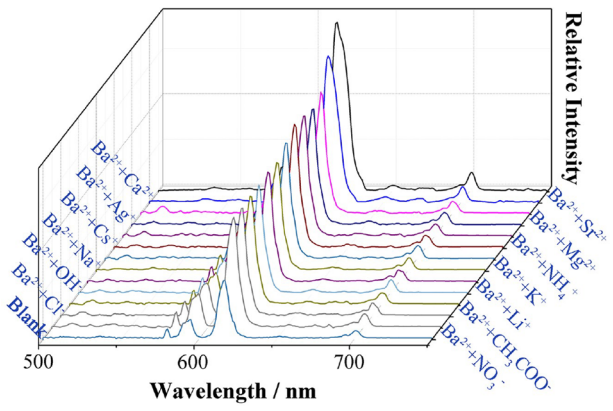

Figure 8. Variation of the FL emission intensity of **1Eu** in aqueous solution containing Ba^{2+} and different anions or cations ($[Ba^{2+}]$ = 0.10 mM, the concentration of other anion or cation is 0.10 mM).

FL probe has a good selectivity for the Ba^{2+} detection in a water environment in the absence of Ca^{2+} or Sr^{2+} ions in the water environment.

CONCLUSIONS

In this work, the sulfur-heterocyclic carboxylic acid ligand was first introduced to the Ln^{3+}-containing POT system and

https://dx.doi.org/10.1021/acs.inorgchem.0c00223
Inorg. Chem. 2020, 59, 6839−6848

constructs two thiophene-dicarboxylic-acid-decorated LCATs **1Eu** and **2Gd**. Intriguingly, the bowknot-like hexameric POA $\{Ln_6W_{14}O_{40}(H_2O)_{18}(Htpdc)_2\}[B\text{-}\alpha\text{-}AsW_9O_{33}]_6^{34-}$ in **1Eu** and **2Gd** can be deemed as six trivacant Keggin $[B\text{-}\alpha\text{-}AsW_9O_{33}]^{9-}$ bridged by a *S*-shaped $[Ln_6W_{14}O_{40}(H_2O)_{18}(Htpdc)_2]^{20+}$ central cluster. **1Eu** can be used to work as a FL probe material for the Ba^{2+} detection in the absence of Ca^{2+} or Sr^{2+} ions in water environment with high sensitivity, good selectivity, and low LOD (1.19×10^{-3} mM). All in all, this work not only creatively introduces S-heterocyclic carboxylic acid ligand into the POM system and enriches the types of organic ligands that can be studied in POM chemistry but also broadens the application of POM-based materials in the FL detection field.

■ ASSOCIATED CONTENT

Supporting Information

The Supporting Information is available free of charge at https://pubs.acs.org/doi/10.1021/acs.inorgchem.0c00223.

Related structural figures; PXRD patterns; IR spectra; related luminescence spectra and lifetime decay curves; TG curves; and UV absorption spectra (PDF)

Accession Codes

CCDC 1976141−1976142 contain the supplementary crystallographic data for this paper. These data can be obtained free of charge via www.ccdc.cam.ac.uk/data_request/cif, or by emailing data_request@ccdc.cam.ac.uk, or by contacting The Cambridge Crystallographic Data Centre, 12 Union Road, Cambridge CB2 1EZ, UK; fax: +44 1223 336033.

■ AUTHOR INFORMATION

Corresponding Authors

Lijuan Chen − *Henan Key Laboratory of Polyoxometalate Chemistry, College of Chemistry and Chemical Engineering, Henan University, Kaifeng, Henan 475004, China*; Email: ljchen@henu.edu.cn

Junwei Zhao − *Henan Key Laboratory of Polyoxometalate Chemistry, College of Chemistry and Chemical Engineering, Henan University, Kaifeng, Henan 475004, China*; orcid.org/0000-0002-7685-1309; Email: zhaojunwei@henu.edu.cn

Authors

Dan Wang − *Henan Key Laboratory of Polyoxometalate Chemistry, College of Chemistry and Chemical Engineering, Henan University, Kaifeng, Henan 475004, China*

Yamin Li − *Henan Key Laboratory of Polyoxometalate Chemistry, College of Chemistry and Chemical Engineering, Henan University, Kaifeng, Henan 475004, China*

Yan Zhang − *Henan Key Laboratory of Polyoxometalate Chemistry, College of Chemistry and Chemical Engineering, Henan University, Kaifeng, Henan 475004, China*

Xin Xu − *Henan Key Laboratory of Polyoxometalate Chemistry, College of Chemistry and Chemical Engineering, Henan University, Kaifeng, Henan 475004, China*

Yong Liu − *Henan Key Laboratory of Polyoxometalate Chemistry, College of Chemistry and Chemical Engineering, Henan University, Kaifeng, Henan 475004, China*

Complete contact information is available at: https://pubs.acs.org/10.1021/acs.inorgchem.0c00223

Author Contributions

All authors have given approval to the final version of the manuscript.

Notes

The authors declare no competing financial interest.

■ ACKNOWLEDGMENTS

This work was supported by the National Natural Science Foundation of China (21671054, 21871077, 21571048, 21771052), the Program for Innovation Teams in Science and Technology in Universities of Henan Province (20IRTSTHN004), the Program of First-Class Discipline Cultivation Project of Henan University (2019YLZDYJ02), and the Postgraduate Education Innovation and Quality Improvement Plan of Henan University (SYL18060130).

■ REFERENCES

(1) Fang, W.-H.; Zhang, L.; Zhang, J. Synthetic strategies, diverse structures and tuneable properties of polyoxo-titanium clusters. *Chem. Soc. Rev.* **2018**, *47*, 404−421.

(2) Li, B.; Fan, H.-T.; Zang, S.-Q.; Li, H.-Y.; Wang, L.-Y. Metal-containing crystalline luminescent thermochromic materials. *Coord. Chem. Rev.* **2018**, *377*, 307−329.

(3) Wang, Z.; Gupta, R. K.; Luo, G.-G.; Sun, D. Recent progress in inorganic anions templated silver nanoclusters: synthesis, structures and properties. *Chem. Rec.* **2019**, *19*, 1−15.

(4) Blanc, A.; de Frémont, P. When gold cations meet polyoxometalates. *Chem. - Eur. J.* **2019**, *25*, 9553−9567.

(5) Li, X.-X.; Zhao, D.; Zheng, S.-T. Recent advances in POM-organic frameworks and POM−organic polyhedra. *Coord. Chem. Rev.* **2019**, *397*, 220−240.

(6) Li, T. F.; Miras, H. N.; Song, Y.-F. Polyoxometalate (POM)-layered double hydroxides (LDH) composite materials: design and catalytic applications. *Catalysts* **2017**, *7*, 260.

(7) Blasco-Ahicart, M.; Soriano-López, J.; Carbó, J. J.; Poblet, J. M.; Galan-Mascaros, J. R. Polyoxometalate electrocatalysts based on earth-abundant metals for efficient water oxidation in acidic media. *Nat. Chem.* **2018**, *10*, 24−30.

(8) Xia, C. X.; Zhang, S. S.; Sun, D.; Jiang, B. L.; Wang, W. S.; Xin, X. Coassembly of mixed Weakley-type polyoxometalates to novel nanoflowers with tunable fluorescence for the detection of toluene. *Langmuir* **2018**, *34*, 6367−6375.

(9) Lu, J.; Kang, Q.; Xiao, J. H.; Wang, T.; Fang, M.; Yu, L. Luminescent, stabilized and environmentally friendly $[EuW_{10}O_{36}]^{9-}$-Chitosan films for sensitive detection of hydrogen peroxide. *Carbohydr. Polym.* **2018**, *200*, 560−566.

(10) Guo, Y. X.; Gong, Y. J.; Qi, L. B.; Gao, Y. A.; Yu, L. A polyoxometalate-based supramolecular chemosensor for rapid detection of hydrogen sulfide with dual signals. *J. Colloid Interface Sci.* **2017**, *485*, 280−287.

(11) Wei, H. B.; Zhang, J. L.; Shi, N.; Liu, Y.; Zhang, B.; Zhang, J.; Wan, X. H. A recyclable polyoxometalate-based supramolecular chemosensor for efficient detection of carbon dioxide. *Chem. Sci.* **2015**, *6*, 7201−7205.

(12) Li, Y. M.; Li, H. L.; Jiang, J.; Chen, L. J.; Zhao, J. W. Three types of distinguishing l-alanine-decorated and rare-earth-incorporated arsenotungstate hybrids prepared in a facile one-step assembly strategy. *Inorg. Chem.* **2019**, *58*, 3479−3491.

(13) Chen, L.; Chen, W.-L.; Wang, X.-L.; Li, Y.-G.; Su, Z.-M.; Wang, E.-B. Polyoxometalates in dye-sensitized solar cells. *Chem. Soc. Rev.* **2019**, *48*, 260−284.

(14) Dubal, D. P.; Chodankar, N. R.; Kim, D.-H.; Gomez-Romero, P. Towards flexible solid-state supercapacitors for smart and wearable electronics. *Chem. Soc. Rev.* **2018**, *47*, 2065−2129.

(15) Li, Q. Y.; Zhang, L.; Dai, J. L.; Tang, H.; Li, Q.; Xue, H. G.; Pang, H. Polyoxometalate-based materials for advanced electro-

chemical energy conversion and storage. *Chem. Eng. J.* **2018**, *351*, 441−461.
(16) Genovese, M.; Lian, K. Polyoxometalate modified inorganic−organic nanocomposite materials for energy storage applications: A review. *Curr. Opin. Solid State Mater. Sci.* **2015**, *19*, 126−137.
(17) Zhang, J. W.; Huang, Y. C.; Li, G.; Wei, Y. G. Recent advances in alkoxylation chemistry of polyoxometalates: from synthetic strategies, structural overviews to functional applications. *Coord. Chem. Rev.* **2019**, *378*, 395−414.
(18) Bijelic, A.; Aureliano, M.; Rompel, A. Polyoxometalates as potential next-generation metallodrugs in the combat against cancer. *Angew. Chem., Int. Ed.* **2019**, *58*, 2980−2999.
(19) Zhao, J.-W.; Li, Y.-Z.; Chen, L.-J.; Yang, G.-Y. Research progress on polyoxometalate-based transition-metal−rare-earth heterometallic derived materials: synthetic strategies, structural overview and functional applications. *Chem. Commun.* **2016**, *52*, 4418−4445.
(20) Zhang, Y. T.; Gan, H. M.; Qin, C.; Wang, X. L.; Su, Z. M.; Zaworotko, M. J. Self-assembly of goldberg polyhedra from a concave $[WV_5O_{11}\ (RCO_2)_5(SO_4)]^{3-}$ building block with 5-fold symmetry. *J. Am. Chem. Soc.* **2018**, *140*, 17365−17368.
(21) Reinoso, S.; Giménez-Marqués, M.; Galán-Mascarós, J. R.; Vitoria, P.; Gutiérrez-Zorrilla, J. M. Giant crown-shaped polytungstate formed by self-assembly of Ce^{III}-stabilized dilacunary Keggin fragments. *Angew. Chem., Int. Ed.* **2010**, *49*, 8384−8388.
(22) Zheng, Q.; Vilà-Nadal, L.; Lang, Z. L.; Chen, J. J.; Long, D. L.; Mathieson, J. S.; Poblet, J. M.; Cronin, L. Self-sorting of heteroanions in the assembly of cross-shaped polyoxometalate clusters. *J. Am. Chem. Soc.* **2018**, *140*, 2595−2601.
(23) Zheng, S.-T.; Zhang, J.; Li, X. X.; Fang, W. H.; Yang, G. Y. Cubic polyoxometalate-organic molecular cage. *J. Am. Chem. Soc.* **2010**, *132*, 15102−15103.
(24) Han, Q.; Li, Z.; Liang, X. M.; Ding, Y.; Zheng, S.-T. Synthesis of a 6-nm-long transition-metal−rare-earth-containing polyoxometalate. *Inorg. Chem.* **2019**, *58*, 12534−12537.
(25) Li, Z.; Li, X.-X; Yang, T.; Cai, Z.-W.; Zheng, S.-T. Four-Shell Polyoxometalates featuring high-nuclearity Ln_{26} clusters: structural transformations of nanoclusters into frameworks triggered by transition-metal ions. *Angew. Chem., Int. Ed.* **2017**, *56*, 2664−2669.
(26) Wang, Y.-J.; Wu, S.-Y.; Sun, Y.-Q.; Li, X.-X.; Zheng, S.-T. Octahedron-shaped three-shell Ln_{14}-substituted polyoxotungstogermanates encapsulating a W_4O_{15} cluster: luminescence and frequency dependent magnetic properties. *Chem. Commun.* **2019**, *55*, 2857−2860.
(27) Ibrahim, M.; Mereacre, V.; Leblanc, N.; Wernsdorfer, W.; Anson, C. E.; Powell, A. K. Self-assembly of a giant tetrahedral 3d−4 f single-molecule magnet within a polyoxometalate system. *Angew. Chem., Int. Ed.* **2015**, *54*, 15574−15578.
(28) Liu, J. C.; Luo, J.; Han, Q.; Cao, J.; Chen, L. J.; Song, Y.; Zhao, J. W. Coexistence of long-range ferromagnetic ordering and spin-glass behavior observed in the first inorganic−organic hybrid 1-D oxalate-bridging nona-Mn^{II} sandwiched tungstoantimonate chain. *J. Mater. Chem. C* **2017**, *5*, 2043−2055.
(29) Li, Z.; Lin, L.-D.; Yu, H.; Li, X.-X.; Zheng, S.-T. All-inorganic ionic porous material based on giant spherical polyoxometalates containing core-shell K_6@K_{36}-water cage. *Angew. Chem., Int. Ed.* **2018**, *57*, 15777−15781.
(30) Liu, J.-C.; Han, Q.; Chen, L.-J.; Zhao, J.-W.; Streb, C.; Song, Y.-F. Aggregation of giant cerium−bismuth tungstate clusters into a 3D porous framework with high proton conductivity. *Angew. Chem., Int. Ed.* **2018**, *57*, 8416−8420.
(31) Han, Q.; Liu, J.-C.; Wen, Y.; Chen, L.-J.; Zhao, J.-W.; Yang, G.-Y. Tellurotungstate-based organotin−rare-earth heterometallic hybrids with four organic components. *Inorg. Chem.* **2017**, *56*, 7257−7269.
(32) Jin, L.; Li, X.-X.; Qi, Y.-J.; Niu, P.-P.; Zheng, S.-T. Giant hollow heterometallic polyoxoniobates with sodalite-type lanthanide−tungsten−oxide cages: discrete nanoclusters and extended frameworks. *Angew. Chem., Int. Ed.* **2016**, *55*, 13793−13797.
(33) Huang, L.; Wang, S.-S.; Zhao, J.-W.; Cheng, L.; Yang, G.-Y. Synergistic combination of multi-Zr^{IV} cations and lacunary Keggin germanotungstates leading to a gigantic Zr_{24}-cluster-substituted polyoxometalate. *J. Am. Chem. Soc.* **2014**, *136*, 7637−7642.
(34) Han, X.-B.; Li, Y.-G.; Zhang, Z.-M.; Tan, H.-Q.; Lu, Y.; Wang, E.-B. Polyoxometalate-based nickel clusters as visible light-driven water oxidation catalysts. *J. Am. Chem. Soc.* **2015**, *137*, 5486−5493.
(35) Kortz, U.; Al-Kassem, N. K.; Savelieff, M. G.; Al Kadi, N. A.; Sadakane, M. Synthesis and characterization of copper-, zinc-, manganese-, and cobalt-substituted dimeric heteropolyanions, $[(\alpha\text{-}XW_9O_{33})_2M_3(H_2O)_3]^{n-}$ (n = 12, X = As^{III}, Sb^{III}, M = Cu^{2+}, Zn^{2+}; n = 10, X = Se^{IV}, Te^{IV}, M = Cu^{2+}) and $[(\alpha\text{-}AsW_9O_{33})_2WO(H_2O)\text{-}M_2(H_2O)_2]^{10-}$ (M = Zn^{2+}, Mn^{2+}, Co^{2+}). *Inorg. Chem.* **2001**, *40*, 4742−4749.
(36) Kortz, U.; Savelieff, M. G.; Bassil, B. S.; Dickman, M. H. A large, novel polyoxotungstate: $[As^{III}_6W_{65}O_{217}(H_2O)_7]^{26-}$. *Angew. Chem., Int. Ed.* **2001**, *40*, 3384−3386.
(37) Wassermann, K.; Dickman, M. H.; Pope, M. T. Self-assembly of supramolecular polyoxometalates: the compact, water-soluble heteropolytungstate anion $[As^{III}_{12}Ce^{III}_{16}(H_2O)_{36}W_{148}O_{524}]^{76-}$. *Angew. Chem., Int. Ed. Engl.* **1997**, *36*, 1445−1448.
(38) Boskovic, C. Rare earth polyoxometalates. *Acc. Chem. Res.* **2017**, *50*, 2205−2214.
(39) Wassermann, K.; Pope, M. T. Large cluster formation through multiple substitution with lanthanide cations (La, Ce, Nd, Sm, Eu, and Gd) of the polyoxoanion $[(B\text{-}\alpha\text{-}AsO_3W_9O_{30})_4(WO_2)_4]^{28-}$. Synthesis and structural characterization. *Inorg. Chem.* **2001**, *40*, 2763−2768.
(40) Hussain, F.; Conrad, F.; Patzke, G. R. A gadolinium-bridged polytungstoarsenate(III) nanocluster: $[Gd_8As_{12}W_{124}O_{432}(H_2O)_{22}]^{60-}$. *Angew. Chem., Int. Ed.* **2009**, *48*, 9088−9091.
(41) Hussain, F.; Patzke, G. R. Self-assembly of dilacunary building blocks into high-nuclear $[Ln_{16}As_{16}W_{164}O_{576}(OH)_8(H_2O)_{42}]^{80-}$ (Ln = Eu^{III}, Gd^{III}, Tb^{III}, Dy^{III}, and Ho^{III}) polyoxotungstates. *CrystEngComm* **2011**, *13*, 530−536.
(42) Liu, Y. J.; Li, H. L.; Lu, C. T.; Gong, P. J.; Ma, X. Y.; Chen, L. J.; Zhao, J. W. Organocounterions-assisted and pH-controlled self-assembly of five nanoscale high-nuclear lanthanide substituted heteropolytungstates. *Cryst. Growth Des.* **2017**, *17*, 3917−3928.
(43) Luo, J.; Jin, G. F.; Zhang, F.; Liu, Y.; Chen, L. J.; Xie, S. Q.; Zhao, J. W. Three types of mixed alkali-metal-, transition-metal-, or rare-earth-substituted sandwich-type arsenotungstates with supporting rare-earth pendants. *Eur. J. Inorg. Chem.* **2018**, *2018*, 143−152.
(44) Hussain, F.; Gable, R. W.; Speldrich, M.; Kögerler, P.; Boskovic, C. Polyoxotungstate-encapsulated Gd_6 and Yb_{10} complexes. *Chem. Commun.* **2009**, 328−330.
(45) Li, H. F.; Wu, H. C.; Wan, R.; Wang, Y.; Ma, P. T.; Li, S. Z.; Wang, J. P.; Niu, J. Y. Utilizing the adaptive precursor $[As_2W_{19}O_{67}(H_2O)]^{14-}$ to support three hexanuclear lanthanoid-based tungstoarsenate dimers. *Dalton Trans.* **2019**, *48*, 2813−2821.
(46) Wang, Y.; Sun, X. P.; Li, S.; Ma, P. T.; Niu, J. Y.; Wang, J. P. Generation of large polynuclear rare earth metal-containing organic−inorganic polytungstoarsenate aggregates. *Cryst. Growth Des.* **2015**, *15*, 2057−2063.
(47) Vonci, M.; Akhlaghi Bagherjeri, F.; Hall, P. D.; Gable, R. W.; Zavras, A.; O'Hair, R. A. J.; Liu, Y.; Zhang, J.; Field, M. R.; Taylor, M. B.; Du Plessis, J.; Bryant, G.; Riley, M.; Sorace, L.; Aparicio, P. A.; López, X.; Poblet, J. M.; Ritchie, C.; Boskovic, C. Modular molecules: site-selective metal substitution, photoreduction, and chirality in polyoxometalate hybrids. *Chem. - Eur. J.* **2014**, *20*, 14102−14111.
(48) Li, H.-L.; Liu, Y.-J.; Liu, J.-L.; Chen, L.-J.; Zhao, J.-W.; Yang, G.-Y. Structural transformation from dimerization to tetramerization of serine-decorated rare-earth-incorporated arsenotungstates induced by the usage of rare-earth salts. *Chem. - Eur. J.* **2017**, *23*, 2673−2689.
(49) Wang, J.; Ma, P. T.; Li, S. J.; Xu, Q. F.; Li, Y. G.; Niu, J. Y.; Wang, J. P. Polyoxotungstate cluster species connected by glutamic acid and europium. *Inorg. Chem.* **2019**, *58*, 57−60.

https://dx.doi.org/10.1021/acs.inorgchem.0c00223
Inorg. Chem. 2020, 59, 6839−6848

(50) Healey, M. R.; Gable, R. W.; Ritchie, C.; Boskovic, C. Accessing yttrium−polyoxometalate−carboxylate hybrids from a versatile arsenotungstate(III) precursor. *Polyhedron* **2013**, *64*, 13−19.
(51) Han, Q.; Sun, X. P.; Li, J.; Ma, P. T.; Niu, J. Y. Beat over the old ground with new strategy: engineering As···As interaction in arsenite-based Dawson cluster β-$[W_{18}O_{54}(AsO_3)_2]^{6-}$. *Inorg. Chem.* **2014**, *53*, 2006−2011.
(52) Yang, P.; Lin, Z. G.; Alfaro-Espinoza, G.; Ullrich, M. S.; Rat, C. I.; Silvestru, C.; Kortz, U. 19-Tungstodiarsenate(III) functionalized by organoantimony(III) groups: tuning the structure−bioactivity relationship. *Inorg. Chem.* **2016**, *55*, 251−258.
(53) Zhao, J.-W.; Li, H.-L.; Ma, X.; Xie, Z. G.; Chen, L.-J.; Zhu, Y. S. Lanthanide-connecting and lone-electron-pair active trigonal-pyramidal-AsO_3 inducing nanosized poly(polyoxotungstate) aggregates and their anticancer activities. *Sci. Rep.* **2016**, *6*, 26406.
(54) Yamase, T. Photo- and electrochromism of polyoxometalates and related materials. *Chem. Rev.* **1998**, *98*, 307−325.
(55) Cui, Y. J.; Yue, Y. F.; Qian, G. D.; Chen, B. L. Luminescent functional metal−organic frameworks. *Chem. Rev.* **2012**, *112*, 1126−1162.
(56) Xu, X.; Chen, Y. H.; Zhang, Y.; Liu, Y. F.; Chen, L. J.; Zhao, J. W. Rare-earth and antimony-oxo clusters simultaneously connecting antimonotungstates comprising divacant and tetravacant Keggin fragments. *Inorg. Chem.* **2019**, *58*, 11636−11648.
(57) Han, Q.; Wen, Y.; Liu, J.-C.; Zhang, W.; Chen, L.-J.; Zhao, J.-W. Rare-earth-incorporated tellurotungstate hybrids functionalized by 2-picolinic acid ligands: syntheses, structures, and properties. *Inorg. Chem.* **2017**, *56*, 13228−13240.
(58) Yang, Y.; Jiang, F. L.; Chen, L.; Pang, J. D.; Wu, M. Y.; Wan, X. Y.; Pan, J.; Qian, J. J.; Hong, M. C. An unusual bifunctional Tb-MOF for highly sensitive sensing of Ba^{2+} ions and with remarkable selectivities for CO_2/N_2 and CO_2/CH_4. *J. Mater. Chem. A* **2015**, *3*, 13526−13532.
(59) Bhasin, A. K. K.; Chauhan, P.; Chaudhary, S. A novel sulfur-incorporated naphthoquinone as a selective "turn-on" fluorescence chemical sensor for rapid detection of Ba^{2+} ion in semi aqueous medium. *Sens. Actuators, B* **2019**, *294*, 116−122.
(60) Ravichandiran, P.; Subramaniyan, S. A.; Bella, A. P.; Johnson, P. M.; Kim, A. R.; Shim, K. S.; Yoo, D. J. Simple fluorescence turn-on chemosensor for selective detection of Ba^{2+} ion and its live cell imaging. *Anal. Chem.* **2019**, *91*, 10095−10101.
(61) Bhasin, A. K. K.; Chauhan, P.; Chaudhary, S. A novel sulfur-incorporated naphthoquinone as a selective "turn-on" fluorescence chemical sensor for rapid detection of Ba^{2+} ion in semiaqueous medium. *Sens. Actuators, B* **2019**, *294*, 116−122.

https://dx.doi.org/10.1021/acs.inorgchem.0c00223
Inorg. Chem. 2020, 59, 6839−6848